Soft Matter

Accepted Manuscript

ROYAL SOCIETY OF CHEMISTRY

www.rsc.org/softmatter

ARTICLE TYPE www. rsc.org/xxxxxx | XXXXXXXX

A new model for cell division and migration with spontaneous topology changes

Anna Mkrtchyan,[a] Jan Åström,[b‡] and Mikko Karttunen*[c]

Received Xth XXXXXXXXXX 20XX, Accepted Xth XXXXXXXXX 20XX
First published on the web Xth XXXXXXXXXX 200X
DOI: 10.1039/b000000x

Tissue topology, in particular proliferating epithelium topology, is remarkably similar between various species. Understanding the mechanisms that result in the observed topologies is needed for a better insight into the processes governing tissue formation. We present a two-dimensional single-cell based model for cell divisions and tissue growth. The model accounts for cell mechanics and allows cell migrations. Cells do not have pre-existing shapes or topologies. Shape changes and local rearrangements occur naturally as a response to the evolving cellular environment and cell-cell interactions. We show that the commonly observed tissue topologies arise spontaneously from this model. We consider different cellular rearrangements that accompany tissue growth and study their effects on tissue topology.

1 Introduction

During the development of multicellular organisms cells are packed into tissues with various functionality. Having a precise topology is essential for proper tissue development and functioning. One example is the packing of cells in eye lens[1]. Fibre cells in eye lens are tightly packed into hexagonal structures which reduce light scattering. Throughout the tissue development, cell divisions, cell-cell interactions and rearrangements alter tissue topology. Understanding the mechanisms that govern cellular packing in tissues is one of the challenges in developmental biology.

Simple epithelium is commonly used to study cell packing geometries. Epithelium is essentially a monolayer of cells that tightly adhere to each other. Based on the observations on cucumber epithelium, Lewis[2] characterized epithelium topology as mainly hexagonal, with asymmetric distribution of pentagons and heptagons. This topology is often conserved among species[3], which suggests a unified mechanism behind tissue formation. Gibson *et al.*[3] showed that in the absence of large-scale rearrangements a topological model with stochastic cell divisions is sufficient to obtain epithelium topology. Topological models have been used to study effects of cell divisions and division plane orientation on tissue topology[3,4]. Cellular geometry and mechanics, which are not considered in topological models, are known to play role in the packing of cells[5,6] and mechanical properties of tissues[60]. Alternations in cell-cell interactions lead to cellular rearrangements that, in some cases, take place during tissue formation[7,8]. To address these issues, various mechanistic models of tissue at different scales have been proposed. Continuum models describe tissue growth and remodelling, and the macroscopic level based on local intercellular interaction functions[62,63]. Mechanical vertex models[9–11] treated tissues as networks of cells. In these models, cells are considered to be polygons in the junctional network. Vertex models have been used to explore the impact of cell mechanics, rearrangements and growth rate on proliferating epithelium topology[9,10,12,13]. They, however, do not take into account cell migrations.

Collective cell migrations are common in various biological processes[14,15]. Along with cell shape changes, they are an essential part of embryonic morphogenesis[16,17,58,59]. Directed cell migrations involve coordinated cycles of protrusion, contraction and adhesion that are regulated by the actomyosin cortex[18,57]. As in the case of cell division, migration also depends on the mechanics of the cell[20] and, in fact, cell motility can be achieved by cortical contraction alone[21,22]. Moreover, comparison between cell morphogenesis and the associated mechanical properties for cell divisions and migrations suggests common regulatory mechanisms that govern cortex remodelling in both cases[23].

A more realistic way to model cell shapes and their mechanical properties requires treatment of individual cells. Individually modelled cells do not carry pre-existing shapes and topologies. Cellular Potts models regard each cell as a collection of spins with energy functional that characterizes cell mechanics and intercellular interaction. An extended Potts model suggested in a seminal work by Graner and Glazier[48,49] considered cell's elasticity and cell-cell interactions to predict

[a] *Department of Applied Mathematics, University of Western Ontario, London, Ontario, Canada*
[b] *CSC Scientific Computing Ltd, Esbo, Finland*
[c] *Department of Chemistry & Waterloo Institute of Nanotechnology, University of Waterloo, Waterloo, Ontario, Canada, E-mail: mkarttu@gmail.com*

cell sorting. Cellular Potts models have since been utilized to explain cell packing topologies[6,57], collective cell motility[53], and tumor growth[61]. Dirichlet models[50–52] reproduce the polygonal shapes of cells by considering the distribution of their centres' of mass in space. Drasdo *et al.* modelled cells as colloidal objects capable of growth, division and migration. The model was used to analyse morphologies of monolayers, multi-cellular spheroids and tissue layers under different growth conditions[24,25], but it did not consider the influence of cell morphologies on tissue formation. Palsson and Othmer[26] presented a model, where cells are treated as deformable viscoelastic ellipsoids. Their model predicts cellular morphologies due to cell-cell signalling and collective migration. The viscoelastic model proposed by Rejniak *et al.*[27] describes cells as an incompressible fluid immersed within elastic boundaries. Growth of the trophoblast bilayer, tumor development and the development of epithelial acini were among the applications of the model[27–29]. Another subcellular element model developed by Newman[30] present a cell as a cloud of mass points that bind to each other. Newman *et al.* focused on the dynamics of multicellular system[31–33].

In this work, we present a single-cell based mechanical model which accounts for cell's cortex contractility and cell-cell adhesion. Each cell is assigned internal pressure, which controls cell growth. The choice of the growth mechanism is inspired by the observations that mitotic cells modulate internal hydrostatic pressure before mitosis[34]. Changes in cell shapes and their local rearrangements are governed by the interplay between cortex contractility, adhesion and internal pressure governs. Individual treatment of cells allows to alter physical properties and growth mechanisms of cells on a single cell level. Additionally, modelling of individual cells provides a way to control the extent of local rearrangements. We show that our model can reproduce commonly observed tissue topologies. We also consider the extent of cellular rearrangements and study their effects on tissue topology.

2 Model and Methods

In this section, we describe the model and provide the computational details used in the simulations. A model for an isolated cell is developed first. That cell is then embedded in a tissue where it interacts with its neighboring cells. These interactions are modelled through repulsion, adhesion, and viscous damping. Importantly, the cells are able to grow, divide and migrate.

2.1 Model

2.1.1 Isolated Cell. A single cell is modelled as a closed loop of mass points connected through springs. Our starting point is the model originally proposed by Åström and Karttunen in their studies of cell aggregation in a confined space[35]. We use this model as the basis and extend it to include cell division and migration.

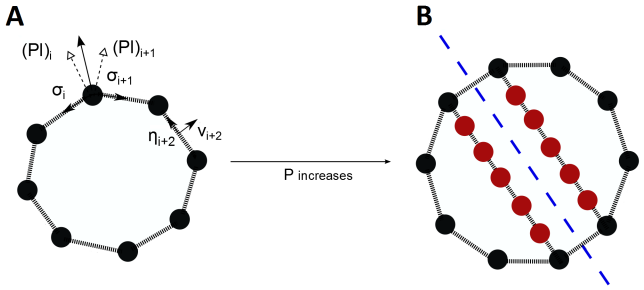

Fig. 1 Mass-spring model for a cell. (A) Forces acting on mass point i in an isolated cell are the spring tension forces (σ_i and σ_{i+1}) and the pressure forces ($(Pl)_i$ and $(Pl)_{i+1}$). A cell grows by gradually increasing its pressure force. (B) Cell divides through a random division line (dashed blue line). During the division, new mass points (red) are added along the division line.

Each mass point experiences tension forces from the two neighbor springs as shown in Fig. 1A. These tension forces define the cell actomyosin cortex's contractility that favours a rounded structure for an isolated cell[34,36]. Each cell is also assigned an internal pressure P. The pressure force is opposed by the spring tension forces from the two nearest neighbors. With the above, the net force acting on mass point i belonging to an isolated cell is given as

$$\vec{F}_i^{cell} = \sigma_i \vec{\eta}_i - \sigma_{i+1}\vec{\eta}_{i+1} + \frac{Pl}{2}(\vec{v}_i + \vec{v}_{i+1}), \qquad (1)$$

where $\vec{\eta}_i$ and $\vec{v}_i$ are the tangential and normal vectors, σ_i is the tension force and Pl represents pressure force, Fig. 1 (A). For a linear elastic spring, tension is given as $\sigma_i = K_i^{spr}(l - l_0)$, where l_0 and l are give equilibrium and instantaneous lengths of springs, respectively. For simplicity, we assume that all cells are identical and homogeneous, i.e., all springs have the same spring constant $K_i^{spr} \equiv K^{spr}$.

2.1.2 Cell in tissue. Next, we place the cell as described above in a tissue, i.e., we define its interactions with other cells. Inside the tissue each mass point is subject to additional forces that arise due to cell-cell interactions. We model them using three terms: 1) repulsion, 2) adhesion, and 3) viscous damping.

1. Repulsion: In order to prevent cells from penetrating into each other, we use spring-like repulsion forces

$$\vec{F}_{ij}^{rep} = \begin{cases} -K^{rep}(R_c^{rep} - R_{ij})\hat{R_{ij}} & \text{if } R_{ij} < R_c^{rep} \\ 0 & \text{otherwise.} \end{cases} \qquad (2)$$

Two mass points are considered to be in contact if they are within a distance R_c^{rep} from each other.

The repulsion force should be strong enough to counteract the pressure force Pl pushing the mass points of a cell into the interior of one (or more) of its neigboring cells. In addition, cell rigidity needs to be taken into account for estimating the repulsion force. Rigidity may vary at the different stages of the cell cycle[37], and since the displacement of the mass points depends on the strength of the spring forces, more rigid cells require stronger repulsion forces. Taking the two above factors into account, we can estimate the numerical value for the repulsion force coefficient to be

$$K^{rep} \sim K^{spr} Pl. \tag{3}$$

2. Adhesion: Tissue integrity is maintained by adhesion between the neighbor cells. Cells adhere to each other through adhesive molecules, often located in specific areas known as cell junctions[38]. In our model, each mass point acts as a potential site for adhesive interaction. When two mass points i and j that belong to different cells are within the interaction distance R_c^{adh}, they attract each other through linear spring-like forces

$$\vec{F}_{ij}^{adh} = \begin{cases} K_{ij}^{adh}(R_c^{adh} - R_{ij})\hat{R_{ij}} & \text{if } R_{ij} < R_c^{adh} \\ 0 & \text{otherwise.} \end{cases} \tag{4}$$

Cells can bind through several binding mechanisms with different associated binding free energies[39]. A realistic treatment of cell-cell adhesion should consider the differences between the adhesion sites, and K_{ij}^{adh} should be different for different mass point pairs. Here we assume that all adhesive sites are identical with the adhesion spring constant $K_{ij}^{adh} \equiv K^{adh}$.

Adhesion favours cell-cell contacts and tends to flatten the neighboring cell surfaces, whereas cell cortex contractility favours a rounded cell structure[36]. We can estimate the relation between the adhesion and contractility spring constants by using the preferred cell shapes inside a tissue. Majority of cells in a proliferating epithelium assume hexagonal shapes[3]. The change of the shape from circular to hexagonal is accompanied by work done against the contractile springs. In the absence of internal pressure forces, this work is compensated by the energy stored in the adhesive springs $W^{spr} \sim W^{adh}$. To estimate the work required to deform the cell (W^{spr}), we assume that the cell has the shape of a regular hexagon with an incircle of radius r. The total change in the perimeter can then be estimated as $\Delta L = L_{hex} - L_{cir} = 12/\sqrt{3}r - 2\pi r$. The total deformation is the result of the deformation of N springs. Hence, the deformation of each spring is equal to $\Delta x = \Delta L/N$. The total energy associated with the deformation of springs can be estimated as $W^{spr} \sim NK^{spr} \cdot (\Delta L/N)^2 \sim 10^{-1} K^{spr} r^2/N$. For a hexagonal shape, all mass points are in contact with the mass points of neighbor cells and participate in cell-cell adhesion with the total energy of $W^{adh} \sim NK^{adh} \cdot (R_c^{adh} - R_c^{rep})^2$. Thus

$$K^{adh} \sim \frac{10^{-1} K^{spr} r^2}{N^2 \cdot (R_c^{adh} - R_c^{rep})^2}. \tag{5}$$

Although this analytical estimate does not include the effects of the internal pressure force, it predicts the order of magnitude for K^{adh}. The final calibration of K^{adh} is then done during the simulation.

3. Viscous Damping: Cells can undergo local rearrangements as well as large scale migrations during tissue formation. The extent of these rearrangements depends on the interactions of cells with their exteriors. We can control the amount of cell rearrangements through a viscous damping force that acts between two neighbor cells. Let i and j be two mass points that belong to two different cells in contact. When cells move along each other, the mass point i slides along the mass point j with the relative velocity $\vec{v_{ij}} = \vec{v_i} - \vec{v_j}$. If $\vec{v_{ij}}^{\tau}$ is the tangential component of the relative velocity, then damping force acting on mass point i can be given as

$$\vec{F}_{ij}^{fric} = -\gamma_i \vec{v_{ij}}^{\tau} \tag{6}$$

Furthermore, since we do not consider the cellular environment explicitly, the effect of motion on the viscous cytoplasm is mimicked through an additional viscous damping force with the coefficient c that acts on all mass points.

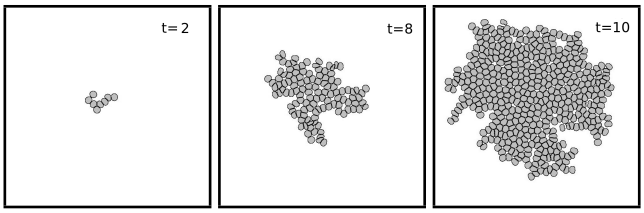

Fig. 2 Snapshots for a simulation at three different times. This growth was started from a single cell at $t = 0$. As time progresses, tissue grows through growth and divisions and the tissue topology changes.

2.1.3 Cell Growth and Division. Animal cells modulate their internal hydrostatic pressures before mitosis[34] and hence we model cell growth by increasing their internal pressure P in a gradual manner. Once the cell area reaches a threshold value A^{div}, the cell divides into two daughter cells. Since the model is scale invariant, we can choose the numerical value for A^{div} to be unity, without any loss of generality. This sets the length scale in our model. During the process of division, new mass points are added along the division line such that the resulting two cells form closed loops and have the same amount of mass points as the initial cell (Fig. 1). To ensure that daughter cells grow similarly to the mother cell, both cells (after a division) are assigned a pressure identical to parent cell. In this work,

we considered division lines which pass through the cells' centres of masses and have random orientation (Fig.1 (B)). Asymmetric cell divisions resulting in daughter cells with different sizes[40] can be incorporated into the model in a straightforward manner.

2.1.4 Cell Migration. Collective cell migrations during embryonic development are an essential part of morphogenesis[16,17]. As a cell migrates, the leading edge extends towards the direction of motion, while the opposite edge retracts[41]. We can model migration by adding a 'migration force' to any mass point to mimic forces causing the migration. The migration force may vary freely in space and time, and can be set to model any scenario of interest. This force will modulate the internal pressure force acting on the mass points. From the algorithmic point of view one can assign mass point to be 'leading edge' or 'rear edge' by setting their internal pressure to a higher or, correspondingly, lower value than that of the mass points of neighbor cells. As a result, the leading edge extends outwards in the direction of difference pressure force, while the rear edge retracts. Consequently, cell moves generally in the direction of the motion of the leading edge.

2.2 Simulation Details

The system evolves according to the following set of equations of motion,

$$M\ddot{\vec{r}}_i = \vec{F}_i^{cell} + \sum_j \vec{F}_{ij}^{adh} + \sum_j \vec{F}_{ij}^{rep} + \sum_j \vec{F}_{ij}^{fric} - c\vec{v}_i, \qquad (7)$$

where M and $\vec{r}_i$ are the mass and the position of the mass point i, and c is the damping coefficient. The forces are given by Eqs. 1, 4, 2 and 6. The first four terms characterise physical properties of the cell and the cell-cell interactions. The cellular environment is taken into account implicitly through viscous damping with the damping coefficient c as described above.

We use the Verlet algorithm for numerical integration of Eq. 7. The positions and the velocities at each time step are obtained through

$$\vec{r}_i(t+\Delta t) = 2\vec{r}_i(t) - \vec{r}_i(t-\Delta t) + \frac{\vec{F}_i(t)}{m_i}\cdot \Delta t^2 \qquad (8)$$

$$\vec{v}_i(t+\Delta t) = \frac{\vec{r}_i(t+\Delta t) - \vec{r}_i(t)}{\Delta t}. \qquad (9)$$

2.2.1 Simulation Procedure. We start the simulation of tissue growth from a single cell. Initially, the lone cell has a circular shape. As the system evolves according to Eq. (7), the cell changes its shape due to its interactions with the environment, see Fig. 2. At the beginning of the simulation, the initial cell is assigned an initial pressure P_{init}, such that the resulting cell area is about the same as the threshold area A^{div}. Cell growth is achieved by increasing the internal pressure at a constant rate. Currently, all cells have the same internal pressure and the same pressure growth rate. Different pressures and growth rates can be used, but for simplicity and to demonstrate the model, we used same pressures and growth rates. Every T^{div} time steps we check areas for all cells and the ones that have the area exceeding threshold value divide according the the procedure described in Sec. 2.1.3. We discuss the choice of T^{div} in Sec. 2.2.2. Following the procedure above, we grew tissues up to 1500 cells.

We used open boundary conditions to mimic tissue growth in a natural environment. To study the properties of growing tissue, data was typically collected from the central part, which we define as the disc with the radius $R = 0.6R_{max}$, where R_{max} is the longest distance of any cell from the center of mass of the system at the given time.

The results were averaged over four samples in which we applied different initial configurations as follows: A single cell, and clusters of five, ten and twenty cells. Initial configurations of cell clusters were generated by grouping cells together in tissue-like structure. Systems were equilibrated prior the production simulations. We considered systems equilibrated when there were no noticeable changes in cell shapes. Results are reported in dimensionless units. Error bars correspond to standard deviation.

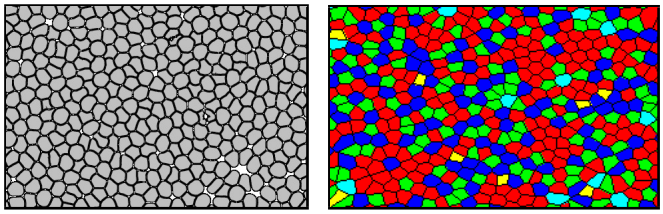

Fig. 3 Two examples of cells in tissue at the end of two separate simulations. *Left*: Snapshot of a simulated tissue. *Right*: Cells shown as polygons through Voronoi tessallation. Different colours indicate different polygon types. The different polygons arise naturally due to cell-cell interactions as described in the text. Pentagons, hexagons and heptagons are coloured as green, red and blue, correspondingly.

2.2.2 Parametrization. Each cell in our model is constructed from N mass points. The numerical value of N should be chosen such that it produces smooth cellular shapes without giving up the computational efficiency. We tested a range of values from $N = 10$ to $N = 200$. Importantly, the results are robust with respect to variation of N as long as N is above ≈ 40. Using larger N does not change the results. The value of $N = 76$ was chosen since it is well above 40 and still computationally efficient; even value was chosen for algorithmic reasons. Thus, $N = 76$ is not a 'magic number'. All mass points have the same mass M. Numerical values for the mass

should be large enough to prevent rapid oscillations of the model springs. At the same time, mass should be small enough such that $M\ddot{\vec{r}}_i \ll 1$. Our simulations show that $M = 0.1$ with the damping coefficient $c = 1$ satisfies both conditions.

Next, we set the threshold area for cell division to unity. With the assumption of circular cell shapes, we can evaluate the distance between the neighboring mass points to be ~ 0.1. The cutoff distance R_c^{rep} for the repulsion force was set to 0.1 as well. The cutoff distance for cell-cell adhesion R_c^{adh} was set to twice of the distance R_c^{rep}.

Division times for the individual cells are characterized by the parameter T^{div}. The choice of T^{div} sets the time scale in our model. Typical cell division time is of order of $\sim$ 1h, while characteristic time for tissue development is ~ 10h[34,42]. Thus, cell division time is roughly 10 times shorter than the time scale of tissue morphogenesis. We pick T^{div} such that the characteristic time for tissue growth and formation in our model is of the order of ~ 1 in reduced units. This leads to T^{div} to be of the order of $\sim 10^{-1}$.

The initial pressure force $P_{init}l$ and cell cortex contractility were chosen such that the resulting cell area was close to the threshold area A^{div}. K^{rep} and K^{adh} were first estimated with the help of Eqs. 3 and 5. We then calibrated these coefficients, along with the pressure force growth rate $\Delta(Pl)$ and damping coefficient for cellular rearrangements γ, by methodically varying these parameters and comparing the resulting tissue topologies with experimental data. The list of computational parameters and their numerical values in dimensionless units are shown in Table 1.

Table 1 List of simulations parameters and their values in dimensionless units

Parameter	Notation	Numerical Value
Mass points per cell	N	76
Mass	M	0.1
Damping of the system	c	1
Equilibrium spring length	l_0	0.1
Cell cortex contractility	K^{spr}	1400
Cell-cell adhesion coefficient	K^{adh}	56
Damping of cellular rearrangements	γ	20
Threshold area	A^{div}	1
Initial pressure force	$P_{init}l$	15
Pressure force growth rate	$\Delta(Pl)$	$5 \cdot 10^{-5}$
Repulsion cutoff distance	R_c^{rep}	0.1
Adhesion cutoff distance	R_c^{adh}	0.2
Simulation time step	Δt	0.0001
Division checkpoints	T^{div}	0.2

To check the model's sensitivity to parameter choices, K^{spr}, $\Delta(Pl)$ and T^{div} were varied. We considered softer springs with values as low as $K^{spr} = 600$, faster growth rates up to $\Delta(Pl) = 5 \cdot 10^{-4}$ and division times down to $T^{div} = 0.1$. We then compared the resulting topologies obtained with the different sets of parameters and found that while at the transient initial stages the topology is somewhat sensitive to the choice of parameters, there are no significant differences within the parameter ranges tested after the initial transient stage.

Next, we provide the relation between the parameters in our model with the experimentally observed physical properties of cells. The parameters in our model are in reduced units, and to define the base for conversion to real units, we matched the model cell mass, diameter and internal pressure force with experimental values.

Typical average cell diameter is about 10μm. The diameter of the cell is set to unity in reduced units. The unit length has the real value of $[l] = 10^{-5}$ m. Cells were chosen to have a mass of an average human cell[43], or 10^{-12} kg. Number of mass points in cell is of order ~ 100. Hence, the total mass of the cell is ~ 10. leading to the mass unit value of $[m] = 10^{-13}$ kg. To estimate the real value of the unit force, we used the experimentally measured value for the pressure force in the mitotic cell based on the work of Stewart *et al.*[34]. The experimental pressure is of the order of $\sim 0.1\,\mathrm{nN}/\mu\mathrm{m}^2$. The reduced pressure force throughout all simulations is of the order $Pl \sim 10 \Rightarrow P \sim 10/l \sim 100[F]/[l]$ in two dimensions. Similarly, the three dimensional pressure in reduced units has the numerical value of $P \sim 100[F]/[l]^2$. Substitution of the real value for the unit length and comparison with the real mitotic pressure leads to the unit of force of $[F] = 10^{-10}$ N. The unit of time is $[t] = \sqrt{[m][l]/[F]} \sim 10^{-4}$ sec. To summarize: the conversions of base units are given as $[m] = 10^{-13}$kg, $[l] = 10^{-5}$ m and $[t] = 10^{-4}$ s. With these definitions, we can compare the physical properties of our model cell with the experimentally observed cell cortex contractility and cell-cell adhesion.

In their experiments with single mitotic cells, Stewart *et al.*[34] evaluated the Young's modulus of mitotic HeLa cells to be of the order of $Y \sim 1\,\mathrm{nN}/\mu\mathrm{m}^2$. $Y \sim 10^3\,[F]\,/\,[l]$ in dimensionless units. The three dimensional Young's modulus is related to the two dimensional as $Y_{2D} \sim 4Y_{3D} \sim 10^3\,[F]\,/\,[l]$. Young's modulus estimated for our model cells can be expressed through spring constant K^{spr} as $Y = K^{spr}l/d$, where l is the spring length and d is the cortex thickness. We set the cortex thickness to be 100 nm[44], or 10^{-2} in reduced units. The numerical value for Young's modulus estimated with our model will then be $Y \sim 10^4\,[F]\,/\,[l]$, roughly 10 times higher than the experimentally observed stiffness for the HeLa cell cortex. This difference of an order of magnitude can be explained by the fact that our model is two dimensional whereas the experimental data is for three dimensional cells. Quantitatively more accurate estimates are expected from the three-dimensional extension of the model (work in progress).

In nature, cell-cell adhesion is mediated by adhesion proteins. Depending on the type of adhesion proteins, protein-ligand binding can have varying binding free energies. The

strength of adhesion depends both on the type of the binding proteins and their distribution. Protein-ligand binding free energies vary from $5k_BT$ [39,54] up to $35k_BT$ [45], whereas the number of bonds per unit area has been estimated to be in the range of $100-1000$ bonds/μm^2 [24,45,55,56]. Taking the average binding energy as $25k_BT$, we calculate the binding energy density to be $2.5\cdot10^{-18}-2.5\cdot10^{-17}$J/$\mu$m^2. Let's use $2.5\cdot10^{-17}$J/μm^2 for further calculations. Conversion to reduced units gives $2.5\,[F]\,/\,[l]$. For lower bond density this is an order of magnitude smaller. Adhesion energy per single bond used in our simulations was $W^{adh} \sim K^{adh}\cdot(R_c^{adh}-R_c^{rep})^2 \sim 0.56\,[F]\,/\,[l]$. The unit length has 10 bonds, and thus the binding energy density in our model is $5.6\,[F]\,/\,[l]$. Thus, the above comparison shows that the adhesion energy used in simulations is very similar to naturally occuring values. Finally, we compare the time scale in our model with the time scale of tissue growth in *Drosophila* wing imaginal disc. The time scale that characterizes tissue growth in our model can be estimated as the simulation time necessary to form a relatively stable configuration of nearest neighbors. It takes roughly 25 division cycles, or 5 reduced time units, for a number of cell neighbors to stabilize. In model units, the units for both damping and time are set to one. *Drosophila* wing imaginal disc growth and formation has the characteristic time of $\sim$ 10h, and the cytoplasmic viscosity, which corresponds to c is about 10^3Pa·s [42,46]. Rescaling the model parameters reveals that, for computational efficiency, there is a speed up of the growth rate by roughly a factor 10 compared to *Drosophila* wing disc.

3 Results

Although many isolated cells prefer spherical shapes, cells in tightly connected tissues assume polygonal shapes due to cell-cell interactions [2,3]. The number of sides of the polygon is defined by the number of the nearest neighbor cells. Thus, to characterize cell topology in tissue, one can assign each cell a polygon type based on the number of its nearest neighbors. For instance a cell with n nearest neighbors can be considered as an n-sided polygon. In this approximation, tissue is considered as polygonal network.

This resemblance has served as the basis for vertex models [9,10]. Stable configurations of epithelial junctional network throughout proliferation, and the ability to incorporate cell mechanics and proliferation, has made vertex models an attractive choice for studying tissue topology. However, cellular shapes lack detailed modelling and intercellular spaces are not captured in these models. Additionally, vertex models do not account for cell migrations and cannot change their initial topologies.

In this work, we consider tissue growth starting from one or a few cells that start to grow and divide (Fig. 2). During the tissue growth, polygonal shapes arise naturally as a result of cell-cell interactions and topologies can change during the course of the time evolution (Fig. 3(*left*)). To characterize the emerging polygon types in our model, we determine the centres of masses of all cells and use them to construct a Voronoi tessellation at each chosen time. Figure 3(*right*) shows an example.

We calculated the fraction of n-sided cells at every 10 time steps and recorded the cell topology distribution. Polygon types change dramatically at the early stages. After about 25 division cycles, the distribution of polygons stabilizes. Most of the cells assume shapes of 4- to 8-sided polygons, but small fractions of 3- and 9-sided polygons also exists. Figure 4 shows the time evolution.

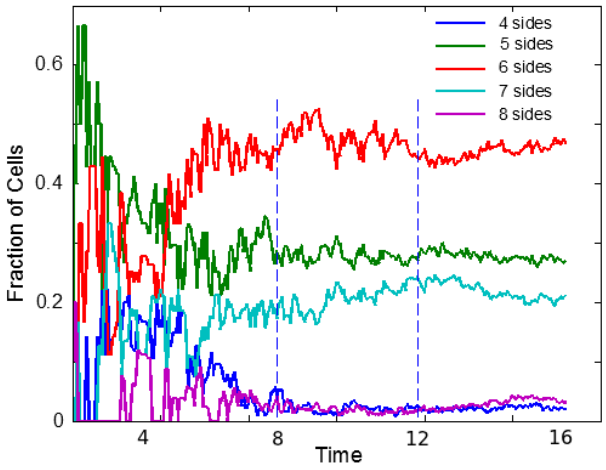

Fig. 4 Time evolution of the polygon distribution. The blue dashed vertical lines show the time interval when the tissue has a mitotic index similar to proliferating epithelium in Drosophila wing disk [47].

Next, we measured the mitotic index. It measures the fraction of cells that divide at a given time. The mitotic index is higher at the initial stages of tissue development when the growth is faster [42], but for most of the epithelial proliferation stays relatively constant at about 1.7% [47]. As tissue approaches its functional size, proliferation ceases.

The mitotic index changes throughout the simulation as well. We measured the mitotic index in our simulations to identify the time intervals during which tissue is in the proliferation regime as defined by experiments. The blue dashed line in Figure 4 shows the regime of proliferating tissue where mitotic index is approximately 1.5% with a standard deviation of 1%. We compare the polygon distribution in proliferating tissue with the experimentally observed tissue topology, Figure 5. As Fig. 5 shows, our model captures the main characteristics of the experimentally observed tissue topology. The distribution has a peak for hexagonal cells and is asymmetric with a slightly higher number of pentagons than heptagons.

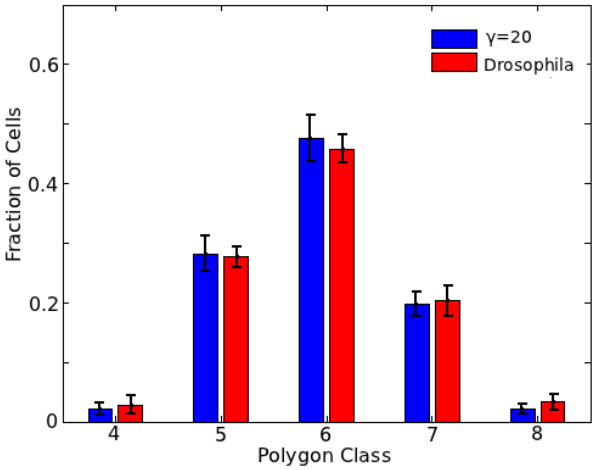

Fig. 5 Polygon type distribution for friction $\gamma = 20$ compared with experimentally observed topology of *Drosophila* wing epithelium topology. Simulation data is averaged for four samples. Error bars indicate standard deviation over all four samples. Experimental data is from the work by Gibson et al.[3]

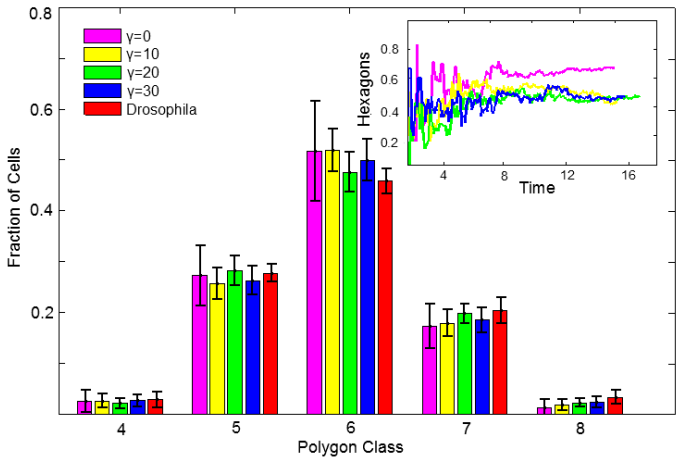

Fig. 6 Polygon type distribution for various cell rearrangements. All four cases reproduce the characteristic polygon distributions in proliferating tissue. Error bars present standard deviation. *Inset* Time evolution of hexagonal cells for one simulation sample.

Finally, we investigated the effect of the damping coefficient γ on tissue topology. As discussed in the Sec. 2.1.2, the damping coefficient γ influences cellular rearrangements. We considered four different cases for γ, Fig. 6. In all four cases, the model reproduced characteristic polygon type distributions of *Drosophila* wing disc[3]. The inset shows the time evolution of hexagonal cells. This measure was chosen since proliferation introduces disorder in the preferred hexagonal packing, and the time evolution of hexagonal cells is correlated with the mitotic rate[3].

A closer inspection of tissue growth reveals that γ affects the growth mechanism. Figure 7 shows snapshots of simulated tissues with two different γ parameters. The two systems had the exact same initial conditions and the two snapshots were taken at the same time. As Figure 7 shows, $\gamma = 0$ leads to a more ordered packing structure as compared to $\gamma = 20$. Importantly, the two cases have different growth mechanism: One can see from Figure 6 (*inset*) that $\gamma = 0$ case has consistently higher percentage of hexagonal cells throughout the entire simulation. Since proliferation introduces disorder into the otherwise optimally packed structure[3], higher percentage of hexagonal cells reflects lower proliferation rate. When $\gamma = 0$, the cells were able to move freely along each other and rearrange themselves close to optimal packing at the early stages of growth. The growth of the central part of the tissue is then restricted by surrounding cells and overall tissue growth is mainly localized within a few outer cell layers. This inhomogeneous growth quickly terminates cell divisions inside the tissue and in the absence of proliferation, leads to optimal hexagonal packing.

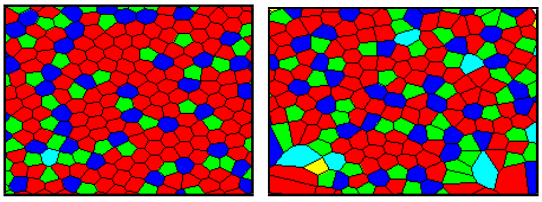

Fig. 7 Snapshots of tissue for two different γ parameteres, i.e., different cellular rearrangements. The two systems were started from the same exact initial conditions and the snapshots were taken at the same time. The resulting polygon types are coloured as green for pentagons, red for hexagons and blue for heptagons correspondingly. $\gamma = 0$ case (*left*), where cellular rearrangements are not suppressed. Cellular packing is shifted toward hexagons, compared with the $\gamma = 20$ case, where the amount of cellular rearrangements is restricted.

4 Conclusions

We have developed a two-dimensional mechanical model for cell divisions and tissue formation. In contrast to vertex models, where polygonal cells are defined as a part of the existing network, we treat each cell independently of its neighbors, which makes it more realistic. In our model, we consider cell cortex contractility and cell-cell adhesion. Cell growth is controled by internal pressure. The model accounts for several cellular processes, including proliferation through various division mechanisms, cell polarity and migrations.

We show that our model reproduces commonly observed

proliferating tissue topologies. We then established a set of parameters that provide a good match with the experimentally observed *Drosophila* wing disc epithelium topology, and compared the numerical values with experimentally measured mechanical properties of cells.

In addition, we considered the effect of damping coefficient γ on tissue growth. We showed that for a wide range of γ, we can reproduce the characteristic distributions of cell polygons, however, different γ lead to different growth mechanism. For $\gamma = 20$, we obtained relatively homogeneous proliferation with the mitotic index 1.5% (compared to the 1.7% of proliferating epithelial mitotic index[47]). For lower values of γ, when cell are moving freely, the tissue displayed inhomogeneous growth: Cellular rearrangements tended to optimize cellular packing at the early stages of tissue development. The growth of tissue then is mainly defined by the growth of the outer cell layer, with almost no proliferation inside the tissue.

In conclusion, we have demonstrated that the two-dimensional model presented here is capable of reproducing the two-dimensional packing topology of developing tissues such as epithelium. Our model can be extended to three-dimensions, where an analogous network of springs models elastic three-dimensional spheroid-like structures that represent cells in three dimensions. Work is in progress to extend the model to three dimensions.

References

1 A. Tardieu and M. Delaye, *Annu. Rev. Biophys. Biophys. Chem.*, 1988, **17**, 47–70.
2 F. T. Lewis, *Anat. Rec.*, 1926, **33**, 331–355.
3 M. C. Gibson, A. B. Patel, R. Nagpal and N. Perrimon, *Nature*, 2006, **442**, 1038–1041.
4 A. B. Patel, W. T. Gibson, M. C. Gibson and R. Nagpal, *PLoS Comput. Biol.*, 2009, **5**, e1000412.
5 T. Hayashi and R. W. Carthew, *Nature*, 2004, **431**, 647–652.
6 J. Käfer, T. Hayashi, A. F. M. Marée, R. W. Carthew and F. Graner, *Proc. Natl. Acad. Sci. USA*, 2007, **104**, 18549–18554.
7 A.-K. Classen, K. I. Anderson, E. Marois and S. Eaton, *Dev. Cell*, 2005, **9**, 805 – 817.
8 J. T. Blankenship, S. T. Backovic, J. S. Sanny, O. Weitz and J. A. Zallen, *Dev. Cell*, 2006, **11**, 459 – 470.
9 L. Hufnagel, A. A. Teleman, H. Rouault, S. M. Cohen and B. I. Shraiman, *Proc. Natl. Acad. Sci. USA*, 2007, **104**, 3835–3840.
10 R. Farhadifar, J.-Ch. Röper, B. Aigouy, S. Eaton and F. Jülicher, *Curr. Biol.*, 2007, **17**, 2095 – 2104.
11 H. Honda, M. Tanemura and T. Nagai, *J. Theor. Biol.*, 2004, **226**, 439 – 453.
12 P. Sahlin and H. Jönsson, *PLoS ONE*, 2010, **5**, e11750.
13 T. Aegerter-Wilmsen, A. C. Smith, A. J. Christen, C. M. Aegerter, E. Hafen and K. Basler, *Development*, 2010, **137**, 499–506.
14 D. A. Lauffenburger and A. F. Horwitz, *Cell*, 1996, **84**, 359–369.
15 D. Hanahan and R. A. Weinberg, *Cell*, 2011, **144**, 646–674.
16 R. Keller and M. Danilchik, *Development*, 1988, **103**, 193–209.
17 M. Chuai, W. Zeng, X. Yang, V. Boychenko, J. A. Glazier and C. J. Weijer, *Dev. Biol.*, 2006, **296**, 137–149.
18 J. A. Theriot and T. J. Mitchison, *Nature*, 1991, **352**, 126–131.
57 W.-T. Chen, *J. Cell Biol.*, 1981, **90**, 187–200.
20 E. Abu Shah and K. Keren, *Curr. Op. Cell Biol.*, 2013, **25**, 550–557.
21 R. J. Hawkins, R. Poincloux, O. Bénichou, M. Piel, P. Chavrier and R. Voituriez, *Biophys. J.*, 2011, **101**, 1041–1045.
22 P. Recho, T. Putelat and L. Truskinovsky, *Phys. Rev. Lett.*, 2013, **111**, 108102.
23 C. Roubinet, P. T. Tran and M. Piel, *Cytoskeleton*, 2012, **69**, 957–972.
24 D. Drasdo, R. Kree and J. S. McCaskill, *Phys. Rev. E*, 1995, **52**, 6635–6657.
25 D. Drasdo, S. Hoehme and M. Block, *J. Stat. Phys.*, 2007, **128**, 287–345.
26 E. Palsson and H. Othmer, *Proc. Natl. Acad. Sci. USA*, 2000, **97**, 10448–53.
27 K. A. Rejniak, H. J. Kliman and L. J. Fauci, *Bull. Math. Biol.*, 2004, **66**, 199–232.
28 K. A. Rejniak, *J. Theor. Biol.*, 2007, **247**, 186 – 204.
29 K. Rejniak and A. Anderson, *Bull. Math. Biol.*, 2008, **70**, 677–712.
30 T. J. Newman, *Math. Biosci. Eng.*, 2005, **2**, 611–622.
31 T. J. Newman, *Multiscale Modeling of Developmental Systems*, Academic Press, 2008, vol. 81, pp. 157 – 182.
32 S. A. Sandersius and T. J. Newman, *Phys. Biol.*, 2008, **5**, 015002.
33 S. A. Sandersius, M. Chuai, C. J. Weijer and T. J. Newman, *PLoS ONE*, 2011, **6**, e18081.
34 M. P. Stewart, J. Helenius, Y. Toyoda, S. P. Ramanathan, D. J. Muller and A. A. Hyman, *Nature*, 2011, **469**, 226–230.
35 J. A. Åström and M. Karttunen, *Phys. Rev. E*, 2006, **73**, 062301.
36 T. Lecuit and P.-F. Lenne, *Nature Rev. Mol. Cell Biol.*, 2007, **8**, 633–644.
37 P. Kunda, A. E. Pelling, T. Liu and B. Baum, *Curr. Biol.*, 2008, **18**, 91–101.
38 B. M. Gumbiner, *Cell*, 1996, **84**, 345–357.
39 G. Weber, *Adv. Protein Chem*, 1975, **29**, 1–83.
40 S. W. Grill, P. Goènczy, E. H. Stelzer and A. A. Hyman, *Nature*, 2001, **409**, 630–633.
41 A. J. Ridley, M. A. Schwartz, K. Burridge, R. A. Firtel, M. H. Ginsberg, G. Borisy, J. T. Parsons and A. R. Horwitz, *Science*, 2003, **302**, 1704–1709.
42 O. Wartlick, P. Mumcu, A. Kicheva, T. Bittig, C. Seum, F. Jülicher and M. González-Gaitán, *Science*, 2011, **331**, 1154–1159.
43 H. Lodish, *Mol. Cell. Biol*, Macmillan, New York, 5th edn, 2008.
44 G. T. Charras, C.-K. Hu, M. Coughlin and T. J. Mitchison, *J. Cell Biol.*, 2006, **175**, 477–490.
45 S. Sarda, D. Pointu, F. Pincet and N. Henry, *Biophys. J.*, 2004, **86**, 3291–3303.
46 V. M. Laurent, E. Planus, R. Fodil and D. Isabey, *Biorheology*, 2003, **40**, 235–240.
47 M. Milán, S. Campuzano and A. García-Bellido, *Proc. Natl. Acad. Sci. USA*, 1996, **93**, 640–645.
48 F. Graner and J. A. Glazier, *Phys. Rev. Lett.*, 1992, **69**, 2013–2016.
49 J. A. Glazier and F. Graner, *Phys. Rev. E*, 1992, **47**, 2128–2154.
50 H. Honda, *J. Theor. Biol.*, 1978, **72**, 523–543.
51 H. Honda, H. Yamanaka, M. Dan-Sohkawa, *J. Theor. Biol.*, 1984, **103**, 423–435.
52 T. Beyer and M. Meyer-Hermann, *Eng. Med. Biol. Mag., IEEE*, 2009, **28**, 38–45.
53 A. Kabla, *J. R. Soc. Interface*, 2012, **9**, 3268–3278.
54 P. C. Weber, J. J. Wendoloski, M. W. Pantoliano and F. R Salemme, *J. Am. Chem. Soc.*, 1992, **114**, 3197–3200.
55 D. Boal, *Cambridge University Press*, Mechanics of the Cell, 2012.
56 J. A. Deeg, I. Louban, D. Aydin, Ch. Selhuber-Unkel, H. Kessler and J. P. Spatz, *Nano Lett.*, 2011, **11**, 1469–1476.
57 N. Chen, J. A. Glazier, J. A. Izaguirre and M. S. Alber, *CPC*, 2007, **176**, 670–681.

58 G. B. Blanchard, A. J. Kabla, N. L. Schultz, L. C. Butler, B. Sanson, N. Gorfinkiel, L. Mahadevan and R. J. Adams, *Nat. Methods*, 2009, **6**, 458–464.
59 L. C. Butler, G. B. Blanchard, A. J. Kabla, N. J. Lawrence, D. P. Welchman, L. Mahadevan, R. J. Adams and B. Sanson, *Nat. Cell. Biol.*, 2009, **11**, 859–864.
60 A. R. Harris, L. Peter, J. Bellis, B. Baum, A. J. Kabla, and G. T. Charras, *Proc. Natl. Acad. Sci. USA.*, 2012, **109**, 16449–16454.
61 A. Shirinifard, J. S. Gens, B. L. Zaitlen, N. J. Popławski, M. Swat and J. A. Glazier, *PLOS ONE*, 2009, **4**, e7190.
62 S. Turner *Phys. Rev. E*, 2005, **71**, 041903.
63 M. Ben Amar, C. Chatelain, and P. Ciarletta, *Phys. Rev. Lett.*, 2011, **106**, 148101.